Journal of Power Sources 581 (2023) 233496

Contents lists available at ScienceDirect

Journal of Power Sources

journal homepage: www.elsevier.com/locate/jpowsour

Ladder-type dihydronaphtho[*1,2,3,4*-rst]pentaphene as building block to construct hole-transporting materials for perovskite solar cells

Dharuman Chandrasekaran [a,1], Shin-Jyun Liou [b,1], Wei-Hao Chiu [c,1], Lee-Che Lee [c], Kun-Mu Lee [c,d,e,**], Yi-Chen Wu [f], Hsien-Hsin Chou [f], Yuan Jay Chang [b,***], Yung-Sheng Yen [a,*]

[a] Department of Chemistry, Chung Yuan Christian University, 320, Zhongli, Taoyuan, Taiwan
[b] Department of Chemistry, Tunghai University, Taichung, 40704, Taiwan
[c] Department of Chemical and Materials Engineering, Chang Gung University, 33302, Taoyuan, Taiwan
[d] Center for Green Technology, Chang Gung University, 33302, Taoyuan, Taiwan
[e] Division of Neonatology, Department of Pediatrics, Chang Gung Memorial Hospital, 33302, Taoyuan, Taiwan
[f] Department of Applied Chemistry, Providence University, 433, Taichung, Taiwan

HIGHLIGHTS

- Three novel hole-transporting materials with DHNP moiety have been synthesized.
- The DHNP is a potential candidate for constructing stable and efficient PSCs.
- The best device performance was the **DC-1**-based device with PCE of 18.09%.

ARTICLE INFO

Keywords:
Hole transporting materials (HTMs)
Perovskite solar cells (PSCs)
Dihydronaphthopentaphene
Polycyclic aromatic hydrocarbon

ABSTRACT

The stability and photovoltaic performance of perovskite solar cells (PSCs) are greatly affected by the use of hole-transporting materials (HTMs). Polycyclic aromatic hydrocarbons (PAHs) are known for their planar structures, which facilitate efficient charge transport and intermolecular interactions, resulting they possess unique electronic and optical properties. In this study, we describe the synthesis of three D−π−D type PAHs-based HTMs compounds (**DC-1**, **DC-2**, and **DC-3**) that contain dihydronaphtho[1,2,3,4-rst]pentaphene (DHNP) as a π conjugation bridge, *p*-methoxy group-substituted arylamine, and diphenylamine-substituted carbazole groups as the donor groups. These DHNP-based molecules can be used as hole-transporting materials in PSCs due to their favorable frontier molecular orbitals (HOMO/LUMO) energy levels. The PSC devices fabricated with **DC-1** yielded a highly efficient power conversion efficiency (PCE) of 18.09%, outperforming those based on **DC-2** (13.21%) and **DC-3** (14.91%), and slightly higher than those using control **spiro-OMeTAD** (16.93%). The proposed novel D−π−D molecules demonstrate potential as HTMs with promising performance for PSCs and contribute to the development of high-efficiency perovskite solar cells.

1. Introduction

Solar energy is considered one of the most promising renewable energy sources, capable of adapting to environmental risks and replacing traditional energy sources like petroleum products [1]. Among various generations of solar cells, perovskite solar cells (PSCs) in the third-generation solar cells gain great attention due to their adaptable fabrication, cost-effectiveness, strong absorbance, long diffusion length and carrier lifetime, low exciton binding energy, and good charge transport mobility [2–5]. Since the groundbreaking work of Miyasaka and co-workers in 2009, perovskite materials have been used as active layers for photovoltaic applications [6]. Until now, the certified power

* Corresponding author.
** Corresponding author. Department of Chemical and Materials Engineering, Chang Gung University, 33302, Taoyuan, Taiwan.
*** Corresponding author.
E-mail addresses: kmlee@mail.cgu.edu.tw (K.-M. Lee), jaychang@thu.edu.tw (Y.J. Chang), ysyen@cycu.edu.tw (Y.-S. Yen).
[1] The first three authors contributed equally to this work.

https://doi.org/10.1016/j.jpowsour.2023.233496
Received 10 May 2023; Received in revised form 25 July 2023; Accepted 5 August 2023
Available online 11 August 2023
0378-7753/

conversion efficiency (PCE) of PSCs is 25.7% to date [7], which was due to the unique photoelectric characteristics of hybrid perovskite crystals, and the use of well-matched interfacial materials [8,9].

Generally, typical PSC devices have four main components: electrodes, hole-transporting materials (HTMs), perovskite sensitizer, and electron transporting materials (ETMs). To achieve high-efficiency perovskite solar cells (PSCs), hole-transporting materials (HTMs) are critical components that allow for efficient extraction of positive charges generated by sunlight [10], making them one of the promising strategies [11]. Besides extracting holes from the active layer and transporting them to the electrode, HTMs are also used as passivation materials to passivate perovskite defects [12–15], as an energy barrier to avoid electrons from being transported to the anode, to isolate moisture to improve device stability, and to increase V_{OC} by matching the HOMO energy level with the energy level of perovskite [16,17].

At present, there are mainly four different types of HTMs have been widely studied in PSCs, namely, inorganic HTMs [18,19], polymer HTMs [20,21], organometallic HTMs [22,23], and organic small molecule HTMs [24,25]. Small molecule HTMs, in particular, have seen extensive development due to their structural designability and simplicity in synthesis and purification. The small organic molecule with a D−π−D architecture has been successfully employed in PSCs because donor groups and/or π-bridge units can be varied to adjust their energy levels. Additionally, these HTMs have well-tailored molecular configurations, good morphology, high hole mobility and conductivity, and relatively low synthetic cost [22]. It is well known that the most widely used organic small molecule HTM for PSCs is **spiro-OMeTAD** [26]. The performance of a PSC device fabricated with **spiro-OMeTAD** can achieve a PCE of over 23.7% [27]. Due to the high production costs of **spiro-OMeTAD**, researchers are making a lot of effort to develop more affordable small organic HTMs. In general, these molecules structure comprised of π-conjugated spacer with arylamine derivatives [28,29], and/or carbazole [30,31] derivatives. Disubstituted carbazole HTMs owing to their electron-donating property and required building blocks for effective HTMs and can improve chemical stability have been also broadly explored recently [32,33].

In recent years, several new materials have emerged as potential HTMs for use in PSCs. One such class of materials that has received significant attention is polyaromatic hydrocarbons (PAHs), due to their unique electronic and optical properties [34,35]. PAHs are renowned for their planar structure, which facilitates efficient charge transport and intermolecular interactions. As a result, they exhibit high carrier mobility and low recombination rates, making them ideal for developing high-performance PSCs. PAHs can significantly improve charge transfer at the interface between the hole-transporting layer and the perovskite active layer. Various types of PAHs have been investigated as potential HTMs, including anthracene [36,37], cyclopenta[hi]aceanthrylene [38], anthradithiophene [39], dihydrodinaphthopentacene [40], pyrene [41], dibenzo[*g*,*p*]chrysene [42], anthanthrone [43], acene [44]. Some PAH-based HTMs have demonstrated power conversion efficiencies (PCEs) of around 21%, which is comparable to or higher than that of **spiro-OMeTAD** [45,46]. However, the search for more economical HTMs with high efficiency and stable devices remains a crucial issue.

With a continued focus on PAHs-based HTMs for PSC applications, we report the synthesis of three new HTMs, **DC-1, DC-2,** and **DC-3**, based on dihydronaphtho[1,2,3,4-rst]pentaphene (DHNP) as a π-spacer with electron-donor groups such as diphenylamines, triphenylamines, and diphenylamine-substituted carbazole. DHNP is a rigid ladder-type π-extended polyaromatic hydrocarbon with a large planar π-conjugated structure, consisting of an anthracene fused with two phenyl groups, which may facilitate intermolecular interaction and enhance the hole transporting ability. We have studied the absorption and emission properties, thermal stability, electrochemical properties, and hole transport abilities of these three novel DHNP-based compounds. We found that the HOMO energy levels of these new HTMs are similar to that of **spiro-OMeTAD** and match well with the valence band of the perovskite (−5.43 eV). Encouragingly, when used as HTMs in n-i-p planar PSCs devices, **DC-1**, **DC-2**, and **DC-3** achieved high PCEs of 18.09%, 13.21%, and 14.91%, respectively, with superior device stability compared to doped **spiro-OMeTAD** (16.93%) under similar conditions. We will discuss the syntheses, characterization, and device performance of these PSCs in detail.

2. Results and discussion

2.1. Synthesis of the materials

The key starting material compound **5** was synthesized by following the literature procedures [47] for the synthesis of ladder compound (**SLMC**) and showed in Scheme 1. Palladium-catalyzed Suzuki coupling reaction between diboron ester-substituted anthracene **2** and **1** afforded the *9,10*-di(*5*-bromo-*4′*-hexylbenzophenon-2yl)anthracene **3**. The diol compound **4** was obtained by reaction *4*-hexylphenyllithium with **3** and then followed by ring closure with boron trifluoride etherate to afford the desired stepladder compound **1** in 82% yield. It is noteworthy that the cyclization reaction can produce syn- and anti-ring cyclization regioisomers. The anti-ring closed isomer would display doublet of doublet signal of 1- and 5-positions aromatic protons of the anthracene unit in the ^{1}H NMR spectrum. However, the ^{1}H NMR spectrum of compound **5** showed a singlet signal at 6.97 ppm which was assigned the protons of 2- and 3-positions of the anthracene unit, indicating it was syn-ring closure product. This result was supported by literature-reported polymer products **SLPPPA** and **LPPPA** containing syn-closed isomers [47], but differed the anti-ring closed isomer **SLMC** compound, although both have similar reaction conditions. The possible formation process of compound **5** was formed intermediate **4A** and then syn-closed to form compound **5**, shown in Fig. S1. In order to try to get the anti-ring closed product, we have attempted to modify the reaction conditions whatever added excess trifluoride etherate, change temperature or reaction time, but the ring-closure reaction still formed the syn-ring closed isomer. Compound **5** is readily soluble in common solvents such as chloroform, tetrahydrofuran, dichloromethane, and toluene.

The synthetic route of **DC-1**, **DC-2**, and **DC-3** are illustrated in Scheme 1. **DC-1** and **DC-3** were obtained from Buchwald-Hartwig cross-coupling reaction between **5** with *4,4′*-dimethoxydiphenylamine (**6**), and N^3,N^3,N^6,N^6-tetrakis(*4*-methoxyphenyl)-9*H*-carbazole-3,6-diamine (**8**). **DC-2** was synthesized by Stille cross-coupling between **5** and *4*-methoxy-*N*-(*4*-methoxyphenyl)-*N*-(*4*-(tributylstannyl)phenyl)benzenamine (**7**). For ease of fabrication of the PSCs devices, these new DHNP-based HTMs are advantageous because they are soluble in most common organic solvents such as DCM, chloroform, tetrahydrofuran, toluene, chlorobenzene, and dichlorobenzene. These three new synthesized compounds were characterized by ^{1}H and ^{13}C NMR and high-resolution mass.

2.2. Optical properties

The UV–Vis absorption spectra of **DC-1**, **DC-2**, and **DC-3** in both solution and thin films are presented in Fig. 1, and the corresponding data are collected in Table 1. The maximum absorption peaks of **DC-1**, **DC-2**, and **DC-3** were observed at 556 nm, 526 nm, and 523 nm, respectively, and were attributed to their intramolecular charge transfer (ICT) character. The bathochromic absorption shift of **DC-1** was attributed to a stronger ICT interaction, whereas the red-shifted absorption observed in **DC-1** to **DC-3**, compared to **spiro-OMeTAD**, was due to the extended π-conjugation length of the anthracene moiety. The thin-film absorption spectra of **DC-1**, **DC-2**, and **DC-3**, as depicted in Fig. 1(b), exhibited a bathochromic shift of 7–13 nm compared to the corresponding solutions, indicating the presence of π–π stacking interactions in the thin-film. The fluorescence spectra of these newly synthesized compounds were measured in DCM solution and are presented in

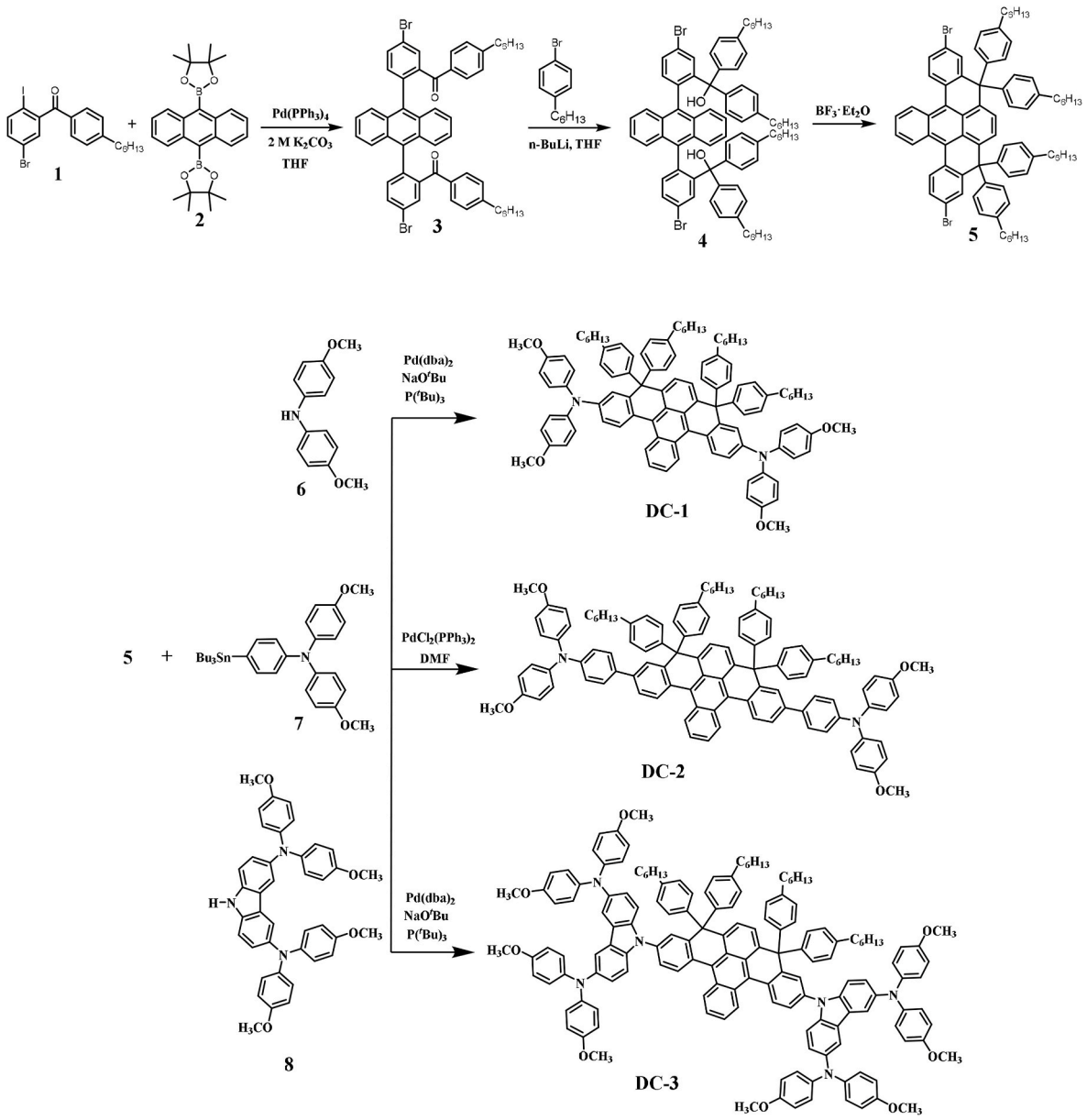

Scheme 1. Synthetic route of **DC**-HTMs.

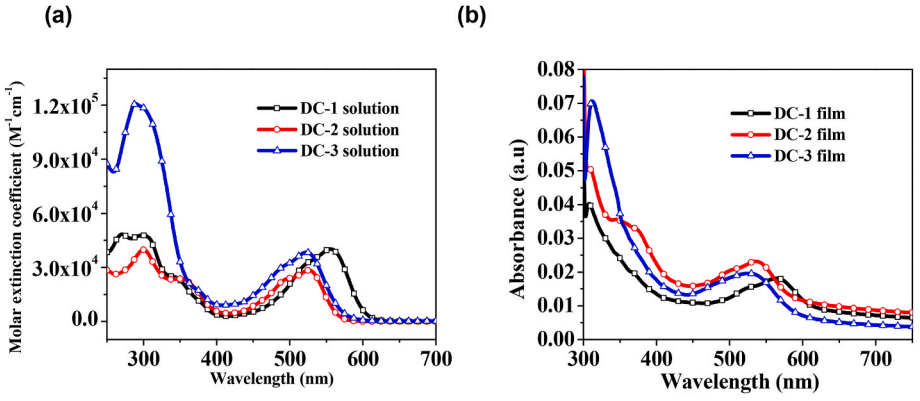

Fig. 1. Absorption spectra of **DC-1**, **DC-2**, and **DC-3** (a) in solution (DCM); (b) in thin film.

Table 1
Photophysical and Electrochemical data of **DC-1, DC-2, DC-3**, and **spiro-OMeTAD**.

HTM	λ^{a}_{max} (soln) ($\varepsilon \times 10^4$ M^{-1} cm^{-1}) (nm)	λ^{b}_{max} (film) (nm)	λ^{a}_{em}(soln) (nm)	$E^{c}_{0\text{-}0}$ (ev)	HOMO/LUMO (eV)	T_d/T^{d}_{g} (°C)	μ^{e}_{h} ($cm^2V^{-1}s^{-1}$)
DC-1	556(4.01)	566	610	2.13	−4.99/-2.85	401/105	4.05×10^{-5}
DC-2	526(2.84)	536	577	2.25	−5.29/-3.05	418/130	1.32×10^{-5}
DC-3	523(3.83)	530	563	2.28	−5.09/-2.81	423/170	2.70×10^{-5}
Spiro-OMeTAD [40]	385(5.24)	396	430	3.04	−5.15/-2.11	422/129	1.49×10^{-5}

[a] Maxima absorption and emission peaks were obtained in dichloromethane. [b] Maxima absorption peaks in the thin film. [c] The value of E_{0-0} was determined from the intersection of absorption and emission spectra. [d] T_d: thermal decomposition temperature, T_g: glass transition temperature. [e] Hole mobilities.

Fig. S2. The emission peaks of **DC-1**, **DC-2**, and **DC-3** were located at 610 nm, 577 nm, and 563 nm, respectively. The Stokes shift values ranged from 40 to 57 nm, supporting the charge-transfer characteristics of the materials. This finding indicates that these HTMs exhibit significant structural deformation in the excited state, which is beneficial for improving pore-filling and enhancing hole extraction ability. The optical energy band-gap for **DC-1**, **DC-2**, and **DC-3**, acquired from the intersection of absorption and emission spectra, was found to be 2.13, 2.25, and 2.28 eV, respectively.

2.3. Electrochemical properties

The alignment of energy levels between the perovskite and HTMs impacts the V_{OC} of the perovskite solar cell. We used electrochemical measurements to calculate the energy levels of these newly synthesized HTMs, and the corresponding data are summarized in Table 1. The representative cyclic voltammograms are shown in Fig. 2(a). As depicted in Fig. 2(a), the first oxidation potentials of **DC** series compounds were attributed to the removal of electrons from arylamine donor groups and were used to estimate the HOMO energy levels. The HOMO values of **DC-1, DC-2**, and **DC-3** were determined to be −4.99 eV, −5.29 eV, and −5.09 eV, respectively, indicating that the trend of donor strength was diphenylamine > diphenylamine-substituted carbazole > triphenylamine. The schematic energy level of **DC-1**, **DC-2**, and **DC-3** is presented in Fig. 2(b). The estimated HOMO values of these HTMs were higher than that of the perovskite valence band (ca. −5.43 eV), indicating that the energy level alignment between the HTMs and perovskite was suitable for hole extraction and transport at the interfacial region. In PSCs, the V_{OC} was determined by calculating the energy difference between the HOMO of HTMs and the Fermi level of the metal oxide, which was used as the electron transport material [48]. **DC-2** has a lower HOMO energy level than **DC-1** and **DC-3**, indicating that it may achieve higher V_{OC} in the PSCs. Moreover, the LUMO energy levels of **DC-1**, **DC-2**, and **DC-3** are higher than the conduction band of $CH_3NH_3PbI_3$ perovskite (−3.93 eV), implying their ability to obstruct electron transfer to the hole transporting layer, thereby preventingcharge recombination [49]. The energy gap of DHNP-based HTMs was reduced compared to **spiro-OMeTAD**, which can be attributed to the introduction of the extended π-conjugate PAHs DHNP segment into the D-π-D structural configuration.

2.4. Thermal stability

Thermodynamic stability of HTM is a crucial factor for the long-term reliability of PSC devices. The thermal gravimetric analysis of **DC-1**, **DC-2**, and **DC-3** also shows high decomposition temperatures (T_d > 400 °C with 5% mass loss), stability of HTMs was determined by thermogravimetric analysis and differential scanning calorimetry, and the relevant data are presented in Table 1. As shown in Fig. S3, the decomposition temperature for **DC-3** (423 °C) is slightly higher than that of **DC-1** (418 °C), **DC-2** (401 °C). Moreover, the thermal gravimetric analysis of **DC-1**, **DC-2**, and **DC-3** also shows high decomposition temperatures (T_d > 400 °C with 5% mass loss), which indicates that these materials are highly thermally stable for use in PSCs. The glass transition temperature (T_g) of **DC-1**, **DC-2**, and **DC-3** are 105 °C, 130 °C, and 170 °C (Fig. S4). The higher T_g of HTMs relative to **spiro-OMeTAD** signifies a more stable amorphous state, which is favorable for the stability of PSC devices.

2.5. Theoretical computation

We conducted theoretical calculations based on density functional theory (DFT) to understand the electronic properties of the HTMs. The optimized ground state molecular geometry and the dihedral angles between DHNP core and arylamine or disubstituted carbazole donors are displayed in Fig. S5 and Fig. S6. As shown in Fig. S6, **DC-3** exhibited a dihedral angle of approximately 49° between the carbazole moiety and central DHNP part, which was larger than that of **DC-1** with diarylamine groups. This larger angle may help to prevent serious aggregation. It is also consistent with **DC-3** having the smallest λ_{max} of ICT band, which is due to the larger dihedral angle. Except for **DC-3**, which has a more twisted DHNP due to the use of a larger disubstituted carbazole donor group (Fig. S5), **DC-1** and **DC-2** exhibited curved planar structure of central aromatic core, which is beneficial for hole mobility. The calculated HOMO energies of **DC-1**, **DC-2**, and **DC-3** were found to be −4.14

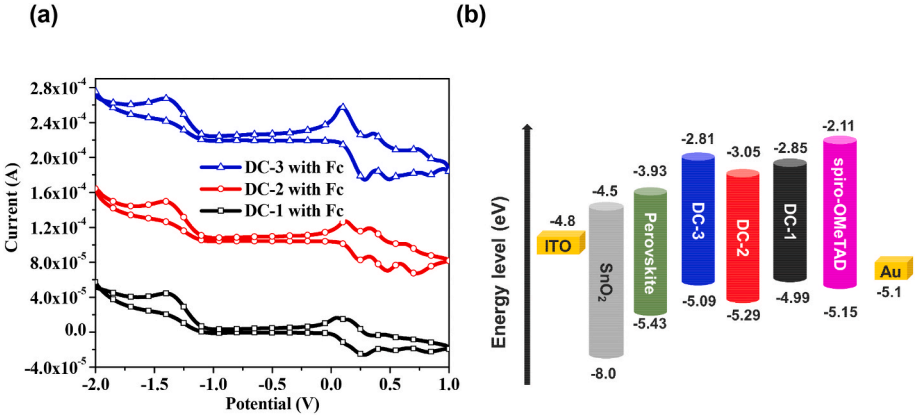

Fig. 2. (a) Cyclic Voltammograms of **DC-1**, **DC-2**, and **DC-3** measured in DCM solution. (b) Energy level diagram of **DC-1**, **DC-2**, **DC-3,** and **spiro-OMeTAD**, and $CH_3NH_3PbI_3$.

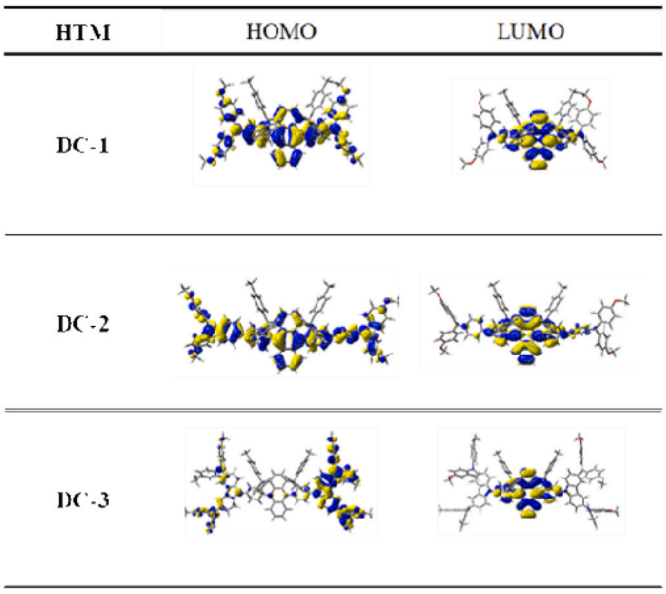

Fig. 3. Frontier orbital distributions for **DC-1**, **DC-2**, and **DC-3**.

eV, −4.36 eV, and −4.24 eV, respectively (Fig. S7), which is consistent with the trend of the experiment results. Fig. 3 illustrates the distribution of the frontier molecular orbitals for **DC-1**, **DC-2**, and **DC-3**. Except for **DC-3**, where the HOMO is mainly localized on one carbazole donor group, the electron distribution of the HOMO in **DC-1** and **DC-2** is mainly delocalized across the entire molecule. Furthermore, the LUMO is localized on the central DHNP core, indicating intramolecular charge transfer for these HTMs, which is beneficial for hole transfer properties.

2.6. Morphology and water contact angle

The cross-section and surface quality of the PSCs with different HTMs spin-coated on perovskite films were employed the scanning electron microscopy (SEM) characterizations to investigate. It is well known that a very smooth and uniform morphology benefits the improvement of the coverage of the hole-transporting layer and helps to reduce grain boundaries. The cross-sectional SEM images in Fig. S8 indicate that **DC-1** and **DC-3** present high-quality films, similar to **spiro-OMeTAD**, while **DC-2** contains multiple pinholes. The top-view SEM images of **DC-1** coated on perovskite films, as shown in Fig. 4, exhibit a uniform HTM layer. In contrast, in **spiro-OMeTAD**-, **DC-2**-, and **DC-3**-based PSCs, some particles were found, and observable pinholes were formed in the **DC-2** and **DC-3** films. We also performed atomic force microscopy (AFM) to investigate the surface roughness of the HTMs and the results showed in Fig. S9. The HTMs were coated on perovskite ($MAPbI_3$), and AFM images were taken with HTMs. The perovskite coated with **DC-1** was show the relative small root mean square (RMS) value (8.81 nm) than **DC-2** (19.17 nm) and **DC-3** (12.15 nm), and similar with **spiro-OMeTAD** (8.81 nm). In conclusion, **DC-1** has relatively good film-forming properties, which are helpful for charge transport and can improve the overall PCE.

HTMs are expected to serve a dual role in improving device stability. Not only do they act as materials for hole extraction and transportation, but they are also expected to create a hydrophobic layer that helps prevent moisture and oxygen infiltration, thus enhancing device stability in humid environments. To evaluate the hydrophobicity of HTMs, contact angle testing was performed on devices with an FTO/perovskite/HTM (doped) structure, and the results are presented in Fig. S10. All the HTMs had a contact angle greater than 80°, which is higher than that of **spiro-OMeTAD** (74.8°). The hydrophobicity of HTMs was observed to decrease in the order of **DC-1** > **DC-2** > **DC-3** > **spiro-OMeTAD**. These results indicate that **DC-1**, **DC-2**, and **DC-3** possess good hydrophobic abilities and can resist water attachment.

Employing the space-charge-limited current (SCLC) method can be useful for investigating the hole-transporting properties, which is another crucial aspect to take into account when developing optimal HTMs for PSCs. Fig. 5(a) illustrates the responses obtained from current-voltage (*J-V*) measurements conducted on hole-only devices featuring an ITO/NiO_x/HTM/MoO_3/Ag structure without any additives. The hole mobility of **DC-1**, **DC-2**, and **DC-3**, and **spiro-OMeTAD** calculated by

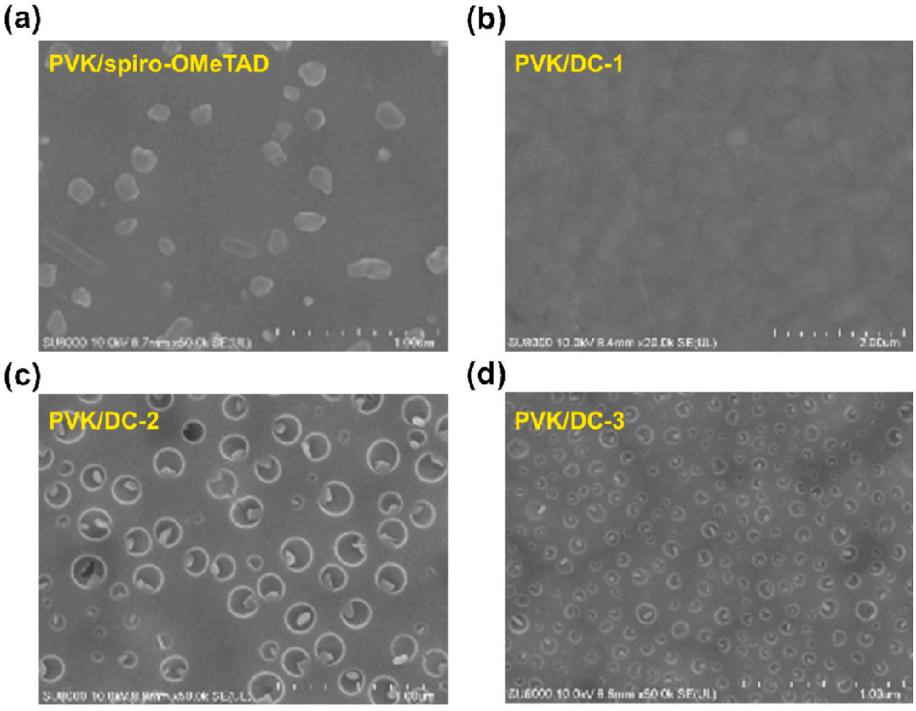

Fig. 4. Top view SEM images of (a) PVK/**spiro-OMeTAD**; (b) PVK/**DC-1**; (c) PVK/**DC-2**; (d) PVK/**DC-3**.

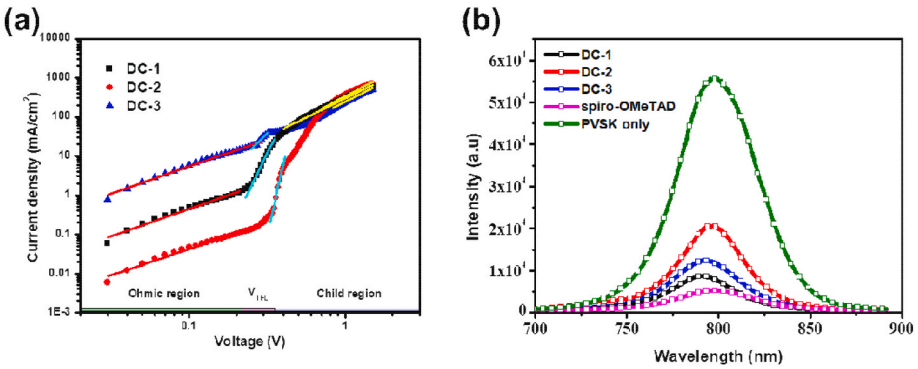

Fig. 5. (a) Hole-mobility investigation for **DC-1**, **DC-2**, and **DC-3**.(b) Steady-state PL spectra of perovskite with and without **DC-1**, **DC-2**, **DC-3**, and **spiro-OMeTAD**.

Mott-Gurney equation is 4.05×10^{-5}, 1.32×10^{-5}, 2.70×10^{-5}, and 1.49×10^{-5} $cm^2V^{-1}s^{-1}$, respectively. Although we expected that using a rigid DHNP conjugated core would be advantageous for hole mobility, the results show that there is no significant increase in hole mobility compared to **spiro-OMeTAD**. Among these newly synthesized HTMs, **DC-1** shows the highest hole mobility due to the smooth film morphology of the **DC-1** film, which effectively conducts photogenerated holes and reduces charge recombination. To assess the ability of perovskite/HTMs to transfer holes, we investigated their steady-state photoluminescence. The PL spectra of perovskite with and without HTM films are displayed in Fig. 5(b). The perovskite/HTM films showed significant photoluminescence (PL) quenching compared to perovskite uncoated with HTM film, which suggests that the holes generated by the excited perovskite layer can be extracted effectively by the HTMs [50]. Among the four HTMs tested, **spiro-OMeTAD** was the most effective in quenching the excited perovskite, while **DC-2** was the least effective due to its poor film-forming. The hole-extracting efficiency of **DC-1** at the interface of perovskite and HTM was the highest and consistent with its photovoltaic performance. Furthermore, we demonstrate that **DC-1** exhibits superior hole-transporting properties, as evidenced by TRPL measurements. The relevant data is presented in Fig. S11 and Table S1. Notably, **DC-1** boasts the shortest average carrier lifetime of 6.98 ns among the HTMs, indicating its remarkable ability to efficiently extract photogenerated holes in the perovskite solar cell.

2.7. Photovoltaic devices

To evaluate the performance of the new DHNP-based small molecules (**DC-1**, **DC-2**, and **DC-3**) as HTMs, PSCs devices were fabricated by employing them in the ITO/SnO_2/perovskite/($MAPbI_3$)/HTM/Au structure. To enhance device performance, lithium bis(trifluoromethanesulfonyl)imide (LiTFSI) and 4-*tert*-butylpyridine (*t*-BP) were added to all cells. The perovskite layer was then spin-coated with HTMs that had been dissolved in chlorobenzene. Cross-sectional SEM was used to image the **spiro-OMeTAD**, **DC-1**, **DC-2**, and **DC-3** based PSCs, as shown in Fig. S8. The SEM images indicate that the HTMs on the perovskite surface were well-covered, and a clear layer-by-layer structure was observed. Fig. 6(a) displays the current-density-voltage (*J-V*) curves of PSCs that use **DC-1**, **DC-2**, and **DC-3** as the HTM and $MAPbI_3$ as the light absorber, measured under simulated solar illumination (AM

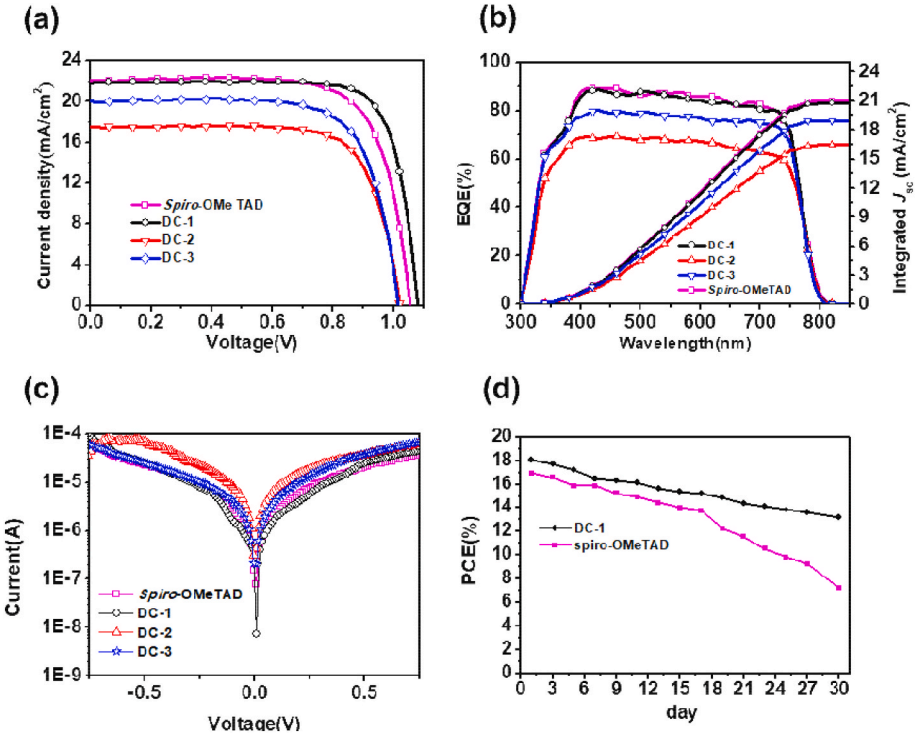

Fig. 6. (a) *J*−*V* curves under AM 1.5 illumination. (b) IPCE spectra for the devices employing doped **DC-1**, **DC-2**, **DC-3**, and **spiro-OMeTAD**. (c) Dark *J-V* curves of the control device. (d) Stability test based on **DC-1** and **spiro-OMeTAD**.

Table 2
Photovoltaic performance of PSCs with doped **DC-1**, **DC-2**, and **DC-3** HTMs and **spiro-OMeTAD**.

HTM	J_{sc} (mA/cm^2)	V_{oc} (V)	FF	PCE(%)	$EQE\_J_{sc}^{b}$ (mA/cm^2)	PCE(%)^c
DC-1	21.89	1.06	0.78	18.09	20.75	17.15
average^a	21.03 ± 0.86	1.05 ± 0.01	0.76 ± 0.02	16.78 ± 1.31		
DC-2	17.51	1.02	0.74	13.21	16.46	12.42
average^a	16.54 ± 0.97	1.00 ± 0.02	0.72 ± 0.02	11.9 ± 1.31		
DC-3	20.03	1.02	0.73	14.91	18.97	14.12
average^a	19.26 ± 0.77	1.00 ± 0.02	0.72 ± 0.01	13.86 ± 1.7		
Spiro-OMeTAD	22.1	1.05	0.73	16.93	20.99	16.09
average^a	19.26 ± 0.77	1.03 ± 0.02	0.71 ± 0.02	15.61 ± 1.32		

[a] Based on 10 PS C devices. (**DC-1** and **DC-3**: 10 mM with 3000 rpm for 30 s; **DC-2**: 30 mM with 2000 rpm for 30s; spiro-OMeTAD: 65 mM with 2000 rpm for 30s) [b] Estimatd from the EQE spectra. [c] Estimated PCE via combining the EQE_J_{sc}.

1.5G, 100 mW cm^{-2}). The photovoltaic parameters of PSC devices, including J_{SC}, V_{OC}, FF, and PCE, are summarized in Table 2.

The power conversion efficiency (PCE) of **DC-1**-based PSCs is 18.09%, the short-circuit current density (J_{SC}) is 21.89 mA cm^{-2}, the open-circuit voltage (V_{OC}) is 1.06 V, and the fill factor (FF) is 0.78. Notably, the PCE of the **DC-1**-based PSCs was significantly higher than those of the **DC-2**-based PSCs (13.21%) and **DC-3**-based PSCs (14.91%). Fig. 6(b) displays the measured EQE spectrum of the device, which indicates an error value of approximately 5–7%. Additionally, we utilized the integrated J_{sc} from EQE to estimate the PCE of the devices, as outlined in Table 2. The calculated PCEs for the PSCs based on **DC-1**, **DC-2**, **DC-3**, and spiro-OMeTAD were found to be 17.15%, 12.42%, 14.12%, and 16.09%, respectively. The observed difference in power conversion efficiency among the PSCs is likely attributable to variations in the film-forming properties of the respective HTMs when coated on the surface of the perovskite layer. Specifically, the film-forming property of the HTM on the perovskite surface may have contributed to the higher PCE observed in the **DC-1**-based PSCs relative to those using **DC-2** and **DC-3**. The SEM image of the surface (Fig. 4) that the **DC-1**-based thin film on $MAPbI_3$ was showed more uniform and smoother than others. The performance of **DC-1**-based PSCs also surpassed the **spiro-OMeTAD**-based device with a PCE of 16.93% (J_{SC} of 22.10 mA cm^{-2}, V_{OC} of 1.05 V, and FF of 0.73) under the same condition. In general, the slightly higher HOMO energy level of **DC-1** than that of **DC-2** and **DC-3** should led to smaller V_{OC} value. However, **DC-1**-based device showed the highest V_{OC} among them. The factors such as carrier mobility, film-forming properties, and charge recombination will affect the V_{OC} in PSCs. To investigate charge carrier recombination, we conducted dark-current measurements (Fig. 6(c)). The reverse current density value of HTMs decrease in the order of **DC-2**≈**DC-3** > **spiro-OMeTAD** > **DC-1**, which is consistent with the trend of the V_{OC} in PSCs. The trap-filled limit voltages (V_{TFL}) of **DC-1**, **DC-2**, and **DC-3** from space-charge limited current measurement were 0.248V, 0.330V, and 0.275 V, respectively. The relatively low V_{TFL} value for **DC-1** based device implied the smaller the trap-state density and will reduce the trap-assisted recombination, resulting in a higher V_{OC} [51]. Therefore, we conjecture the higher V_{OC} and fill factor are dominated by hole mobility and film morphology in this work. Hence, the more uniform film and high mobility of **DC-1**-based PSCs showed the higher V_{OC} and FF in PSCs. Fig. 6(b) displays the monochromatic incident photon-to-current efficiency (IPCE) spectra and the corresponding integrated current density. The IPCE spectra indicate that photocurrent generation begins at about 815 nm, consistent with the band gap of $MAPbI_3$ [52]. The photon-to-current response of the devices ranges from 300 nm to 815 nm. The devices using **DC-1** and **spiro-OMeTAD** have similar spectral responses, which are higher than those of the **DC-2**- and **DC-3**-based cells. As expected, **DC-2** exhibits a relatively lower IPCE response around 380 nm–780 nm region. The integrated J_{SC} of devices with **DC-1**, **DC-2**, **DC-3**, and **spiro-OMeTAD** are 21.89 mA cm^{-2}, 17.51 mA cm^{-2}, 19.33 mA cm^{-2}, and 22.09 mA cm^{-2}, respectively, which are in good agreement with the experimental $J-V$ measurements. The statistical distribution of photovoltaic performance in these three novel HTMs-based PSCs was shown in Fig. S12, the results show that these HTMs-based PSCs have good reproducibility.

For the PSCs, long-term stability is an important issue in terms of commercialization. The long term stability of PSCs based on **DC-1** without encapsulation was monitored at 35% humidity for 30 days. As shown in Fig. 6(d), the **DC-1**-based PSCs maintained close to 80% of initial PCE (18.09%) after 30 days with a PCE of 13.20%, while the efficiency of the **spiro-OMeTAD**-based device decreased remarkably with a PCE of 7.24%. Therefore, the result demonstrates that the **DC-1**-based PSC exhibit better stability compared to **spiro-OMeTAD**, which may be due to the smooth film-forming property preventing the moisture and oxygen.

For commercialization purpose of PSCs, developing cost-effective HTM with good photovoltaic performance properties is a good way to reduce the cost of the PSCs. We have estimated the cost of **DC-1**, and the calculation is shown in Table S2−**S5**. Compared to the cost of spiro-OMeTAD (~400 USD/gram, Sigma-Aldrich), the cost of the best performance HTM **DC-1** is 33.23 USD per gram, which is significantly lower than spiro-OMeTAD. It suggests that using **DC-1** as HTM for PSCs was a relatively low-cost promising candidate material.

3. Conclusion

To summarize, we have synthesized and characterized three new D-π-D type PAHs-based HTMs (**DC-1**, **DC-2**, and **DC-3**) based on a DHNP core structure for potential use in PSCs. The HTMs have similar photophysical, electrochemical, and thermal properties with high thermal stability, making them practical for use in photovoltaic devices. SCLC measurements demonstrated that **DC-1** has higher hole mobility than the other two compounds due to the smoother film morphology. PL quenching result showed that **DC-1** possesses better hole transfer ability. Out of the three HTMs, **DC-1** exhibited the highest PCE (18.09%), surpassing the devices fabricated using **DC-2** (13.21%), **DC-3** (14.91%) and **spiro-OMeTAD** (16.93%) under simulated solar illumination (AM 1.5G, 100mWcm^{-2}). The lower V_{OC} values of **DC-2** and **DC-3** were due to the poor film-forming properties. Overall, DHNP-based HTMs are potential candidates for stable and efficient PSCs, and further modifications to their structure may improve their performance.

4. Experimental section

Materials and Characterization: Unless stated otherwise, all chemical reactions were conducted under an atmosphere of pre-purified nitrogen using Schlenk techniques, and the all commercial materials were used without further purification. THF and toluene used were distilled from Na/benzophenone prior to use. Column chromatography was conducted using glass columns packed with silica gel (60 M, 230–400 mesh). Cyclic voltammetry experiments were conducted using an electrochemical workstation (CHI 611E) with a conventional three-electrode configuration. Absorption and emission spectra were measured with a Jasco V-730 UV–Vis spectrophotometer and Jasco FB-8300 spectrofluorometer, respectively, using dichloromethane as a solvent at room temperature. A

concentration of 1 x 10^{-5} mol mL^{-1} was used for solution UV/visible and PL measurements. ^{1}H and ^{13}C NMR spectra were recorded on a Bruker 400 MHz spectrometer. The thermal decomposition temperature was determined by a Thermal Gravimetric Analyzer (TGA, Q50), and differential scanning calorimetry (DSC) was performed on a NETZSCH DSC 214 Polyma DSC21400A-0324-L under nitrogen atmosphere. Melting points were determined with a Buchi melting point B-540.

Compound **6** [53], **7** [40], and **8** [54] were prepared according to the procedures outlined in the literature method. Compound **5** was synthesized along with the literature method [47].

Fabrication and Characterization of PSCs: An efficient PSC was fabricated with ITO/SnO_2/perovskite/HTM/Au. ITO-conducting glass (ITO glass, Solaronix TCO22-7; sheet resistance = 7 Ω square^{-1}) and a SnO_2 blocking layer was applied on the ITO substrate through a solution process. Deposited the SnO_2 layer on the ITO glass substrate by spin-coating at 3000 rpm for 30 s. Sinter the dense SnO_2 film on a heat plate at 150 °C for 30 min, then cool down for the next step. Afterwards, using a single-step method to produce the perovskite layer. 200 mg of methylammonium iodide and 576 mg of lead iodide was dissolved in 1 mL dimethylformamide and stirred at 60 °C for 8 h. The dense SnO_2 film was spin coated with this solution at 5000 rpm for 30 s and heated on a hot plate for 10 min. After that, a solution composed of HTM (**spiro-OMeTAD**: 65 mM, **DC-1**, **DC-2**, and **DC-3**: 15 mg in 1 mL chlorobenzene), 17.5 μL of lithium bis(trifluoromethanesulfonyl)imide (520 mg in 1 mL CH_3CN) and *4-tert*-butyl pyridine dissolved in acetonitrile and chlorobenzene was spin-coated at 2000 rpm for 30 s to form hole-transporting layer under the N_2 condition. A 100 nm gold electrode was thermally evaporated on the top of the perovskite layer to complete the PSC encapsulation. Scanning electron microscopy (SEM) with a cold-field-emission scanning electron microscope (Hitachi SU8010; acceleration voltage, 0.1–30 kV; working distance, 4.0–6.0 mm) was used to measure the cross-section and surface morphology of the PSCs. The *J–V* curves and IPCE spectra measurements processes were as follows. The devices parameters were obtained under incident light with an intensity of 100 mWcm^{-2} (as measured using a thermopile probe; Oriel 71964) generated by a 300 W solar simulator (Oriel Sol3A Class AAA Solar Simulator 9043A, Newport) and passed through an AM1.5 filter (Oriel 74110). Using an Oriel reference solar cell (Oriel 91150) and adjusted to 1.0 sun (100 mW cm^{-2}) to further calibrated the light intensity. A monochromator (Oriel 74100) under short-circuit conditions was used to record the monochromatic quantum efficiency. A black metal mask (0.09 cm^2) was placed over the devices during the *J–V* and IPCE measurements.

Theoratical computations: The theoretical computations were performed using Gaussian09 package software. To optimize the geometry of the molecules, a hybrid B3LYP functional and 6-31G* basis set were utilized. Excited states were characterized using TD-DFT. Additionally, the frontier orbital plots of the HOMO and LUMO were created with Gauss View 06.

CRediT authorship contribution statement

Dharuman Chandrasekaran: Conceptualization, Data curation, design of study, Writing – original draft, Approval of the version of the manuscript to be published. **Shin-Jyun Liou:** Fabricated and characterized devices, Data curation, acquisition of data. Approval of the version of the manuscript to be published. **Wei-Hao Chiu:** Characterized devices, Data curation, acquisition of data. Approval of the version of the manuscript to be published. **Lee-Che Lee:** Characterized devices, Data curation, acquisition of data. Approval of the version of the manuscript to be published. **Kun-Mu Lee:** Formal analysis, Data curation, Formal analysis, interpretation of data. Approval of the version of the manuscript to be published. **Yi-Chen Wu:** Data curation, acquisition of data. Approval of the version of the manuscript to be published. **Hsien-Hsin Chou:** Formal analysis, Data curation, Formal analysis, Approval of the version of the manuscript to be published. **Yuan Jay Chang:** Writing – review & editing, Formal analysis, Data curation, Formal analysis, Approval of the version of the manuscript to be published. **Yung-Sheng Yen:** Supervision, Conceptualization, Writing – original draft, Approval of the version of the manuscript to be published.

Declaration of competing interest

The authors declare that they have no known competing financial interests or personal relationships that could have appeared to influence the work reported in this paper.

Data availability

Data will be made available on request.

Acknowledgements

This work was financially supported by the Ministry of Science and Technology of Taiwan (111-2113-M-033-006, 111-2113-M-029-008 and 111-2223-E-182-001-MY4). K.-M.L. gratefully acknowledges the financial supports of the Chang Gung University (QZRPD181), and Chang Gung Memorial Hospital, Linkou (CMRPD2M0042).

Appendix A. Supplementary data

Supplementary data to this article can be found online at https://doi.org/10.1016/j.jpowsour.2023.233496.

References

[1] S. Chu, A. Majumdar, Nature 488 (2012) 294–303.
[2] Q. Chen, N. De Marco, Y. Yang, T.B. Song, C.C. Chen, H.X. Zhao, Z.R. Hong, H. P. Zhou, Y. Yang, Nano Today 10 (2015) 355–396.
[3] N.-G. Park, M. Grätzel, T. Miyasaka, K. Zhu, K. Emery, Nat. Energy 1 (2016), 16152.
[4] J.Y. Kim, J.-W. Lee, H.S. Jung, H. Shin, N.-G. Park, Chem. Rev. 120 (2020) 7867–7918.
[5] Q. Lin, A. Armin, R.C.R. Nagiri, P.L. Burn, P. Meredith, Nat. Photonics 9 (2015) 106–112.
[6] A. Kojima, K. Teshima, Y. Shirai, T. Miyasaka, J. Am. Chem. Soc. 131 (2009) 6050–6051.
[7] H. Zhang, X. Ji, H. Yao, Q. Fan, B. Yu, J. Li, Sol. Energy 233 (2022) 421–434.
[8] S.D. Stranks, H.J. Snaith, Nat. Nanotechnol. 10 (2015) 391–402.
[9] J.-P. Correa-Baena, A. Abate, M. Saliba, W. Tress, T. Jesper Jacobsson, M. Grätzel, A. Hagfeldt, Energy Environ. Sci. 10 (2017) 710–727.
[10] Y. Li, H. Xie, E.L. Lim, A. Hagfeldt, D. Bi, Adv. Energy Mater. 12 (2022), 2102730.
[11] J. Seo, J.H. Noh, S.I. Seok, Acc. Chem. Res. 49 (2016) 562–572.
[12] M. Guo, J. Xu, J. Li, J. Huang, J. Zhu, Y. Li, P. Gao, J. Li, M. Wei, J. Mater. Chem. A 11 (2023) 8299–8307.
[13] J. Zhu, Z. Liu, P. Hu, M. Guo, Y. Li, J. Li, M.A. Akram, M. Wei, ACS Sustain. Chem. Eng. 10 (2022) 13825–13834.
[14] J. Zhu, X. Hu, Z. Liu, M. Guo, Y. Zhang, Y. Li, J. Li, M. Wei, J. Mater. Chem. A 11 (2023) 14959–14970.
[15] P. Hu, S. Huang, M. Guo, Y. Li, M. Wei, ChemSusChem 15 (2022), e202200819.
[16] I. Gelmetti, N.F. Montcada, A. Pérez-Rodríguez, E. Barrena, C. Ocal, I. García-Benito, A. Molina-Ontoria, N. Martín, A. Vidal-Ferran, E. Palomares, Energy Environ. Sci. 12 (2019) 1309–1316.
[17] J. Urieta-Mora, I. García-Benito, A. Molina-Ontoria, N. Martín, Chem. Soc. Rev. 47 (2018) 8541–8571.
[18] J. Liang, C. Wang, Y. Wang, Z. Xu, Z. Lu, Y. Ma, H. Zhu, Y. Hu, C. Xiao, X. Yi, G. Zhu, H. Lv, L. Ma, T. Chen, Z. Tie, Z. Jin, J. Liu, J. Am. Chem. Soc. 138 (2016) 15829–15832.
[19] P.K. Kung, M.H. Li, P.Y. Lin, Y.H. Chiang, C.R. Chan, T.F. Guo, P. Chen, Adv. Mater. Interfac. 5 (2018), 1800882.
[20] X.L. Sun, X.Y. Yu, Z.A. Li, ACS Appl. Energy Mater. 3 (2020) 10282–10302.
[21] L. Zhang, C. Liu, J. Zhang, X. Li, C. Cheng, Y. Tian, A.K.Y. Jen, B. Xu, Adv. Mater. 30 (2018), 1804028.
[22] P. Mahajan, B. Padha, S. Verma, V. Gupta, R. Datt, W.C. Tsoi, S. Satapathi, S. Arya, J. Energy Chem. 68 (2022) 330–386.
[23] Z. Yu, A. Hagfeldt, L. Sun, Coord. Chem. Rev. 406 (2020), 213143.
[24] C.H. Teh, R. Daik, E.L. Lim, C.C. Yap, M.A. Ibrahim, N.A. Ludin, K. Sopian, M. A. Mat Teridi, J. Mater. Chem. A 4 (2016) 15788–15822.
[25] P. Murugan, T. Hu, X. Hu, Y. Chen, J. Mater. Chem. A 10 (2022) 5044–5081.
[26] S.-Y. Jeong, H.-S. Kim, N.-G. Park, ACS Appl. Mater. Interfaces 14 (2022) 34220–34227.
[27] H. Min, M. Kim, S.-U. Lee, H. Kim, G. Kim, K. Choi, J.H. Lee, S.I. Seok, Science 366 (2019) 749–753.

[28] S. Park, J.H. Heo, J.H. Yun, T.S. Jung, K. Kwak, M.J. Ko, C.H. Cheon, J.Y. Kim, S. H. Im, H.J. Son, Chem. Sci. 7 (2016) 5517–5522.
[29] A. Farokhi, H. Shahroosvand, G.D. Monache, M. Pilkington, M.K. Nazeeruddin, Chem. Soc. Rev. 51 (2022) 5974–6064.
[30] B. Xu, E. Sheibani, P. Liu, J. Zhang, H. Tian, N. Vlachopoulos, G. Boschloo, L. Kloo, A. Hagfeldt, L. Sun, Adv. Mater. 26 (2014) 6629–6634.
[31] E. Sheibani, L. Yang, J. Zhang, Sol. RRL 4 (2020), 2000461.
[32] W. Yu, Q. Yang, J. Zhang, D. Tu, X. Wang, X. Liu, G. Li, X. Guo, C. Li, ACS Appl. Mater. Interfaces 11 (2019) 30065–30071.
[33] C. Lu, M. Aftabuzzaman, C. Hoon Kim, H. Kyu Kim, Chem. Eng. J. 428 (2022), 131108.
[34] G.-W. Kim, H. Choi, M. Kim, J. Lee, S.Y. Son, T. Park, Adv. Energy Mater. 10 (2020), 1903403.
[35] L. Fang, Y. Zhang, M. Ren, X. Xie, T. Li, Y. Yuan, J. Zhang, P. Wang, Energy Environ. Sci. 15 (2022) 1630–1637.
[36] A. Singh, S.Y. Abate, C. Pavan Kumar, W.-T. Wu, J.-C. Hsiao, F.-L. Wu, J.T.s. Lin, Y.-T. Tao, ACS Appl. Energy Mater. 3 (2020) 10752–10764.
[37] M. Harikrishnan, S. Murugesan, A. Siva, Nanoscale Adv. 2 (2020) 3514–3524.
[38] D. Zhang, P. Xu, T. Wu, Y. Ou, X. Yang, A. Sun, B. Cui, H. Sun, Y. Hua, J. Mater. Chem. A 7 (2019) 5221–5226.
[39] J. Santos, J. Calbo, R. Sandoval-Torrientes, I. García-Benito, H. Kanda, I. Zimmermann, J. Aragó, M.K. Nazeeruddin, E. Ortí, N. Martín, ACS Appl. Mater. Interfaces 13 (2021) 28214–28221.
[40] D. Chandrasekaran, Y.-L. Chiu, C.-K. Yu, Y.-S. Yen, Y.-J. Chang, Chem. Asian J. 16 (2021) 3719–3728.
[41] Y. Ou, A. Sun, H. Li, T. Wu, D. Zhang, P. Xu, R. Zhao, L. Zhu, R. Wang, B. Xu, Y. Hua, L. Ding, Mater. Chem. Front. 5 (2021) 876–884.
[42] X. Zhang, X. Liu, R. Ghadari, M. Li, Z.a. Zhou, Y. Ding, M. Cai, S. Dai, ACS Appl. Mater. Interfaces 13 (2021) 12322–12330.
[43] H.D. Pham, T.T. Do, J. Kim, C. Charbonneau, S. Manzhos, K. Feron, W.C. Tsoi, J. R. Durrant, S.M. Jain, P. Sonar, Adv. Energy Mater. 8 (2018), 1703007.
[44] S. Kazim, F.J. Ramos, P. Gao, M.K. Nazeeruddin, M. Grätzel, S. Ahmad, Energy Environ. Sci. 8 (2015) 1816–1823.
[45] H. Guo, H. Zhang, C. Shen, D. Zhang, S. Liu, Y. Wu, W.H. Zhu, Angew Chem. Int. Ed. Engl. 60 (2021) 2674–2679.
[46] B.X. Zhao, C. Yao, K. Gu, T. Liu, Y. Xia, Y.-L. Loo, Energy Environ. Sci. 13 (2020) 4334–4343.
[47] C. Yang, J. Jacob, K. Müllen, Macromolecules 39 (2006) 5696–5704.
[48] A. Hagfeldt, G. Boschloo, L. Sun, L. Kloo, H. Pettersson, Chem. Rev. 110 (2010) 6595–6663.
[49] P. Qin, N. Tetreault, M.I. Dar, P. Gao, K.L. McCall, S.R. Rutter, S.D. Ogier, N. D. Forrest, J.S. Bissett, M.J. Simms, A.J. Page, R. Fisher, M. Grätzel, M. K. Nazeeruddin, Adv. Energy Mater. 5 (2015), 1400980.
[50] Z.a. Li, Z. Zhu, C.-C. Chueh, S.B. Jo, J. Luo, S.-H. Jang, A.K.Y. Jen, J. Am. Chem. Soc. 138 (2016) 11833–11839.
[51] J.-W. Lee, S.-G. Kim, S.-H. Bae, D.-K. Lee, O. Lin, Y. Yang, N.-G. Park, Nano Lett. 17 (2017) 4270–4276.
[52] B.-X. Chen, H.-S. Rao, W.-G. Li, Y.-F. Xu, H.-Y. Chen, D.-B. Kuang, C.-Y. Su, J. Mater. Chem. A 4 (2016) 5647–5653.
[53] Y. Li, L. Scudiero, T. Ren, W.-J. Dong, J. Photochem. Photobiol., A: Chem 231 (2012) 51–59.
[54] S.D. Sung, M.S. Kang, I.T. Choi, H.M. Kim, H. Kim, M. Hong, H.K. Kim, W.I. Lee, Chem. Commun. 50 (2014) 14161–14163.